RAA 2021 Vol. **21** No. **2**, 40(12pp) doi: 10.1088/1674-4527/21/2/40

http://www.raa-journal.org *http://iopscience.iop.org/raa*

***R**esearch in*
***A**stronomy and*
***A**strophysics*

A new telescope with three fields of view to measure the orientation parameters of the Moon and terrestrial planets

Li-Zao Sun (孙立早)[1,3], Cheng-Li Huang (黄乘利)[2,3], Yong Yu (于涌)[2,3], Zhao-Xiang Qi (齐朝祥)[2,3], Zheng-Hong Tang (唐正宏)[1,3], Ming Zhao (赵铭)[1], De-Hua Yang (杨德华)[4] and Tong Wu (吴彤)[5]

[1] Shanghai Astronomical Observatory, Chinese Academy of Sciences, Shanghai 200030, China
[2] CAS Key Laboratory of Planetary Sciences, Shanghai Astronomical Observatory, Chinese Academy of Sciences, Shanghai 200030, China; *clhuang@shao.ac.cn*
[3] School of Astronomy and Space Science, University of Chinese Academy of Sciences, Beijing 100049, China
[4] College of Automation Engineering, Nanjing University of Aeronautics and Astronautics, Nanjing 211106, China
[5] Key Laboratory of Space Photoelectric Detection and Sensing of Ministry of Industry and Information Technology, College of Astronautics, Nanjing University of Aeronautics and Astronautics, Nanjing 211106, China

Received 2020 April 14; accepted 2020 August 9

Abstract For lots of scientific questions about lunar physics deep inside the Moon, in-situ observation on lunar physical libration is one of the most potential ways. In this paper, we propose a brand new optical telescope functioned with simultaneously observing multiple (here there are three) fields of view (FOVs) for in-situ observation of lunar physical libration. The telescope can be placed at any place with any attitude on the Moon and do not require manned install, control or operation. It passively, continuously and simultaneously observe stars in three FOVs along with rotation of the Moon. Libration is to be measured and studied from celestial motion of the directions of three FOVs from image processing. The concept and design of this telescope are firstly introduced in this paper. The principle and feasibility of the method of in-situ observation are also demonstrated. From simulation, precision of the determined lunar physical libration is expected to be several milliarcsecs, about two orders of magnitude better than the current precision of libration by lunar laser ranging observation. Libration data with milliarcsec precision level can play a valuable role in the study of the physics and dynamics of the interior of the Moon. This telescope can also be applied to observe the rotation of other terrestrial planets like Mars.

Key words: astrometry — telescopes — methods: observational — reference systems

1 INTRODUCTION

The internal physics and structure of planets (including the Moon) are not only directly related to their history of formation and evolution, but also determine their dynamic behavior and destination of later evolution.

As the Earth, people's understanding on its internal structure mainly comes from seismology and normal modes observation, followed by Earth rotation, gravity field, and geomagnetic field observations, etc. For other planets in the solar system, the Mars InSight Lander, jointly developed and launched by the United States and the European Union, landed on Mars in November 2018. Its main scientific purpose is to explore the internal structure and the physics of Mars (Folkner et al. 2018).

For the nearest celestial body to the Earth, what is the structure of the interior of the Moon? Is there surely a liquid outer core and a solid inner core just like the Earth? If so, how big are they? What is the fine structure of the internal density distribution? So far, there is not a very sure answer to these questions and the understanding on the deep interior of the Moon is still superficial and ambiguous.

In lunar seismology study, due to the limitation of the source of the moonquakes, there are not strong enough moonquakes to pass the lunar deep region. There also lacks a necessary globally spreading seismological stations (Lognonné & Johnson 2007). In gravity study, the lunar inner core is not even sure of its existence because it produces signal too weak to be detected currently

(Williams et al. 2014), although the dedicated GRAIL (Gravity Recovery and Interior Laboratory) mission is very successful in detecting the lunar gravity field (Zuber et al. 2013).

The time varied rotation change of the Moon compensating to the Cassini's law is called the lunar physical libration. It is not only the result of the tidal attraction of the major planets (especially the Earth) in the solar system to the Moon's asymmetric mass distribution or equatorial bulge, but also the overall dynamic result of the interaction of the various layers of the Moon.

If high-precision monitoring data of lunar rotation can be obtained and combined with the selenodesy research of moonquake observation, gravity field, remote sensing and telemetry information etc., it is possible to clearly answer the above questions, to promote current focus on geology of the surface of the Moon and to deepen the research on the physics and the dynamics of the Moon's interior.

With lunar rotation (or libration) itself being one of the main contents of the lunar ephemerides (e.g. JPL's LExxx series), the low accuracy of the lunar rotation model is the biggest bottleneck of the current available lunar ephemerides. Any high-precision data on lunar rotation will also possibly solve this long-last problem.

At present, the observation of the rotation of the Moon mainly comes from the lunar laser ranging (LLR) observation which is a technique based on the Earth and measure the apparent ranging of five reflectors on the surface of the Moon (Dickey et al. 1994). Although the ranging precision of LLR can be better than 1 cm now, among all the factors causing variation of the distance between LLR telescope on the Earth and the retro-reflector on the Moon, LLR's sensitivity to the motion tangential to the laser beam is much worse than the sensitivity to the motion along the laser beam due to the limitation of LLR's geometric principle. Consequently the precision of the LLR determined lunar rotation/libration in the directions tangential to the laser beam (or in other word, around the direction of the laser beam) is much worse than the 1 cm ranging precision (Huang et al. 1999). As a result, the precision of rotation parameters of the Moon determined from LLR data is difficult to exceed 0.1 arcsec level, which cannot meet the needs of lunar dynamics research.

One of the best solutions is to monitor the Moon's rotation on its surface (i.e. in-situ observation). In recent years, the National Astronomical Observatory of Japan and JAXA (Japan Aerospace Exploration Agency) have once proposed a lunar attitude measurement program (ILOM) in which they try to put a photographic zenith tube (PZT) at the north pole of the Moon as an attempt to realize in-situ observation of rotation of the Moon (Hanada et al. 2012). Limited by the lunar landing mission, it has not been successfully implemented. Moreover, it is mainly the traditional technique of ground-based optical zenith observation which will be seriously limited by the requirement of observing the network and difficulties in the installation and control of the PZT.

In this paper, we propose a brand new optical telescope with multiple (here there are three) FOVs for in-situ observation of the lunar physical libration. The telescope is proposed to be placed on the Moon at any place with any attitude and do not need manned install, control or operation. It passively, continuously, and simultaneously observes stars in three FOVs along with rotation of the Moon. Libration is to be measured and studied based on data of the celestial motion of the centers of three FOVs from image processing.

The concept and design of this telescope will be firstly introduced in this paper in Section 2. The technical details, including the principle how to distinguish and solve the nutation and the polar motion components of the Moon's rotation from observation will be demonstrated in Section 3. The method and result of the computational test which aims to simulate the in-situ observation will be presented in Section 4.

From simulation, the precision of the determined lunar physical libration can be expected to be at a magnitude of several milliarcsecs (mas), about two orders of magnitude better than the existing LLR measurement precision, which can play a really valuable role in the study of the physics and dynamics of the interior of the Moon. We hope this small telescope can help us in answering the scientific questions mentioned at the beginning of this paper clearly. This telescope can be also applied to observe the rotation of other terrestrial planets like Mars.

2 CONCEPT AND DESIGN OF THE NEW TELESCOPE

A primary discussion on the concept and the design of the new telescope were first presented by Huang et al. (2013, 2015). The project can be accomplished by a brand new designed telescope which will be installed on the surface of the Moon. Its distinction is that the telescope can observe three FOVs simultaneously by only one optical system. It can be realized by placing a trihedron mirror set made of glass ceramic before the pupil of an upside-down telescope like Figure 1.

The mirror set has three slanted reflecting surfaces with a silver coating and faces toward three different sky zones. After being reflected by the corresponding mirror surfaces, star images from three sky zones propagate identically along the optical axis into the telescope and

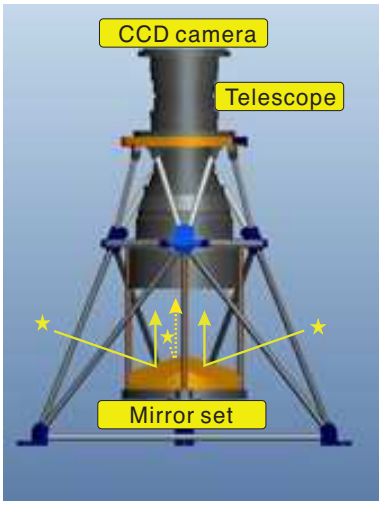

Fig. 1 Schematic of the three field of view (FOV) telescope and propagation of star images from three FOVs. The telescope (*in black*) is installed upside-down with a mirror set (*in yellow*) before its pupil. After being reflected by the corresponding mirror surfaces, star images from three sky zones propagate identically along the optical axis into the telescope.

finally be recorded by the same CCD camera mounted at the end of the telescope.

The star images from three FOVs share the same optical system and the same CCD plate while the observed sky zones in three FOVs are independent. Thus, this special designed three FOVs telescope can be regarded as three independent telescopes which observe the sky zones coincide with their corresponding FOVs. The optical axis of the three equivalent independent telescopes can reversely be regarded as the effective optical axis (EOAs) of the three FOVs as illustrated by Figure 2.

As the angles among the normals of the reflecting surfaces are fixed to given values during construction of the mirror set, the basic angles (ξ_{ij}) among the three EOAs are consequently fixed to $\boldsymbol{P}_i \cdot \boldsymbol{P}_j = \cos\xi_{ij} = \text{const.}$ ($\{i,j\} \in \{A,B,C|i \neq j\}$) and will be used as strong constraints in the afterward data process.

The telescope device has no special requirement for installation such as location, orientation or direction on the surface of the Moon. The directions of EOAs are designed to be fixed and rotating along with rotation of the Moon with its sidereal period of approximate 27.5 days in space except for local deformations caused by physical reasons like the lunar tide. Traces of directions of EOAs in space reveal the rotation of the Moon.

The rotation change of the Moon causes motion of the rotation axis in both the celestial reference frame (CRF) and the selenographic reference frame. For $i = A, B, C$ representing observation of different FOVs, the

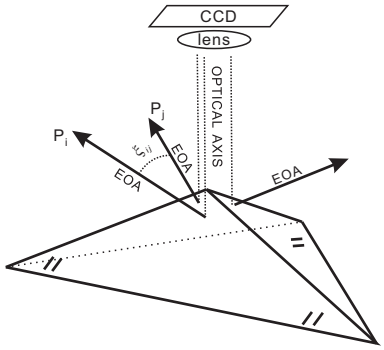

Fig. 2 The mirror set splits the original telescope's optical axis (*dotted lines*) into three corresponding effective optical axes (EOAs). Directions of EOAs in space are constrained by basic angles ξ_{ij} ($\{i,j\} \in \{A,B,C|i \neq j\}$) which are fixed parameters once the mirror set is made and they are key constraints applied in data process. The angle between two EOAs follows $\boldsymbol{P}_i \cdot \boldsymbol{P}_j = \cos\xi_{ij} = \text{const.}$

observational equations are:

$$\boldsymbol{P_i}(t) \cdot \boldsymbol{\omega_0}(t) = \cos\Gamma_i(t), \tag{1}$$

where $\boldsymbol{P_i}(t)$ and $\boldsymbol{\omega_0}(t)$ are the direction of the ith EOA (result of image processing) and the rotation axis of the Moon in CRF at epoch t respectively. $\Gamma_i(t)$ is the angle between the rotation axis and the direction of the ith EOA.

If assume that the rotation axis of the Moon does not change in space within a short time span, the traces of the directions of three EOAs in space would be the concentric circles (Fig. 3). On one hand, the center of the concentric circles corresponds to the position of the rotation axis of the Moon in CRF ($\boldsymbol{\omega_0}$). On the other hand, because the directions of EOAs $\boldsymbol{P_i}(i = A,B,C)$ are fixed in the selenographic frame, the position of the rotation axis in this frame can be determined through $\Gamma_i(i = A,B,C)$.

In a real situation of observation, the position change of the center of the concentric circles in CRF is the precession-nutation of the Moon and the change of $\Gamma_i(t)$ are caused by the polar motion of the Moon. Details about the method of solving the parameters of rotation change of the Moon will be discussed in Section 3.

The main advantages of this new project include:

(1) It is different from the way where observation is made by the absolute measurement of traditional observation techniques like PZT, i. e. the rotation change of the Moon is measured by the motion of the center and change of the radius of the concentric circles of directions of EOAs from observing all the stars in three FOVs, rather than measuring the position of single stars in the selenographic frame. With this method, it greatly reduces technical difficulties when applied to the Moon. Mechanical parts and energy consumption of the system can also be largely reduced.

(2) Three dimensional motion of the Moon in space can

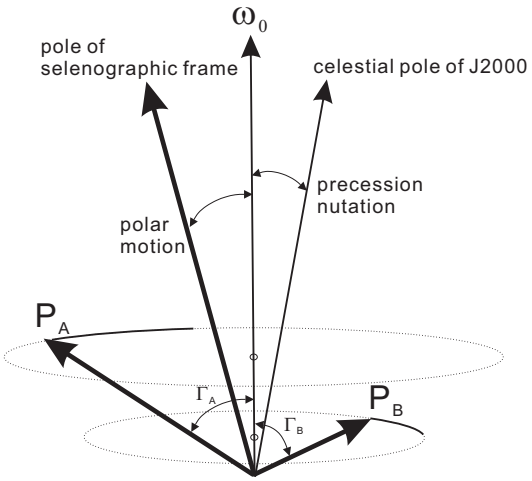

Fig. 3 The direction of the rotation axis of the Moon in CRF ($\boldsymbol{\omega_0}$) and the angles (Γ_i) between the rotation axis and the i-th EOA (P_i) can be determined through traces of directions of EOAs ($\boldsymbol{P}_A$ and $\boldsymbol{P}_B$ here, $\boldsymbol{P}_C$ is omitted). Along with the rotation of the Moon, directions of EOAs draw concentric circles in space. The common center coincides with the rotation axis. With EOA $\boldsymbol{P_i}$ fixed to the selenographic frame (*bold lines*), the position of the rotation axis in this frame can be determined through $\Gamma_i (i = A, B, C)$.

be observed by only one physical telescope system which avoids a global network on the Moon.

(3) This observational method can also be applied to observe rotation of other terrestrial planets like Mars.

3 TECHNICAL DETAILS

3.1 Observation Details

The quantity of FOVs in the observation is balanced between two most factors: First, more observation data can be achieved through more FOVs; second, detecting the ability of the optical system is equally distributed to each FOV. We make a temporary decision that the quantity of FOVs takes three.

Star images from three different FOVs will share the whole CCD plate and mix together because all the FOVs are able to use the entire optical system. To know which FOV an image of a star comes from, the recognition work is based on different motion behavior of star images on the plate which differs with FOVs. The detailed method of star recognition will be discussed in Section 4.3. After recognition, the image at each observational epoch can be restored to three images recorded equivalently by three independent telescopes at the same epoch. Then it can be processed in a standard method of CCD image processing.

For each FOV, the direction of EOA coincides with the respective center of FOV. The size of each FOV is identical to the physical telescope's FOV.

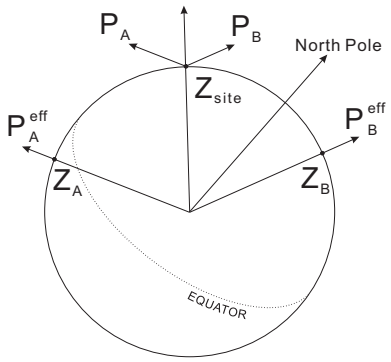

Fig. 4 Ignoring the diurnal parallax in the position of the star and translating the origin of EOAs from the physical site (zenith of the physical site is $Z_{\rm site}$ to the center of the Moon, the observation of three FOVs is equal to three independent telescopes located at Z_A, Z_B and Z_C (omitted here) who observe their respective local zenith. i.e. P_A equals to $P_A^{\rm eff}$ and P_B equals to $P_B^{\rm eff}$.

On the image of each FOV, one can find a point matching to the direction of EOA and the point usually does not change position in the plate frame. Practically we regard the center of the CCD plate as the common corresponding point for images from each FOV.

Deviation of the real corresponding point for each FOV from the plate center will be caused by misalignment during installation but it will not change during observation. Moreover, the change of directions of EOAs in CRF are more concerned than directions of EOAs themselves in principle. Thus the deviation introduced above would not affect.

From celestial positions of star images in one given FOV, we can determine the celestial coordinate of the corresponding point of the EOA. The brief procedure will be discussed in Section 4.2.

Because the radius of the Moon is extremely minor compared with the distance from observer to stars, the magnitude of the diurnal parallax in the position of the star will not exceed 2 microarcsecs. This magnitude of influence in the position of star is not necessary to take consideration in the optical observation. Translating the origins of EOAs from the observation station to the center of the Moon, the direction of one EOA in CRF will coincide with the zenith direction of another *effective observer*. Consequently, directions of three EOAs at one physical site are equal to three corresponding effective observers who observe their local zenith at three other locations on the Moon (Fig. 4).

The geometries among the three EOAs are extremely stable with the low thermal expansion of the mirror set made of glass ceramic (Lindig & Pannhorst 1985). As the Moon's tectonic plate is usually regarded as an entire body, the effective observers whose zenith directions coincide

with directions of EOAs respectively can construct a selenographic reference frame.

Theoretically, observation on the Moon will not be affected by Sun light because of the absence of light scattering from the atmosphere. Although continuous observation can last months, it prefers dividing the observational data series of directions of EOAs in CRF (e.g. data lasts 1 month for each session) and calculate the precession-nutation parameters and the polar motion parameters of the Moon respectively for each session.

3.2 Precession-nutation of the Moon

Precession-nutation of the Moon is referred to as the combined motion of the Moon's rotation axis in space whose periods are usually much longer than 27.5 days. Within one short sampling period, we temporarily ignore the motion of the Moon's rotation axis. Hence, the traces of directions of EOAs are approximately in planes parallel to each other in space.

Direction of the rotation axis in CRF $\boldsymbol{\omega_0}(\bar{X}, \bar{Y}, \bar{Z})$ can be determined by calculating the normal of the paralleled planes. If it represents celestial directions of EOAs in Cartesian coordinate as $\boldsymbol{P_i}(x_{i,t}, y_{i,t}, z_{i,t})$ at observational epoch t where $i = A, B, C$, it can be solved through

$$\bar{X}x_{i,t} + \bar{Y}y_{i,t} + \bar{Z}z_{i,t} + D_i = 0\,. \tag{2}$$

The results are the mean direction of the rotation axis in CRF $(\bar{X}, \bar{Y}, \bar{Z})$ during the sampling period and information on mean angles $(D_i, i = A, B, C)$ between one of the directions of three EOAs and the rotation axis. Because $\bar{Z}$ is very close to 1, it usually makes a simple denotation as $(\bar{X}, \bar{Y}, 1)$.

However, a period of lunar physical libration covers widely from 5 days to 273 years with respect to the inertial space (Rambaux & Williams 2011) and the rotation axis of the Moon is always changing its position in space (Fig. 5). The sampling period which permits processing as Equation (2) would cover a time span much shorter than 1 month if the precision of several mas is expected. The motion of the rotation axis during 1 month can be achieved by numbers of short-time-span data segmentations (which will be further discussed in Sect. 4.4) respectively solved by Equation (2) and then fitted by a model of the pole's motion as

$$X = X_0 + \dot{X}T + \ddot{X}T^2, \tag{3}$$

$$Y = Y_0 + \dot{Y}T + \ddot{Y}T^2. \tag{4}$$

$T = t - t_0$ is time interval between observation epoch (central epoch of each short segmentation) and the central epoch t_0 of the whole one-month data series. Consequently, the result of the direction of the rotation axis of the Moon in CRF at t_0 is $\boldsymbol{\omega}_0(X_0, Y_0, 1)$.

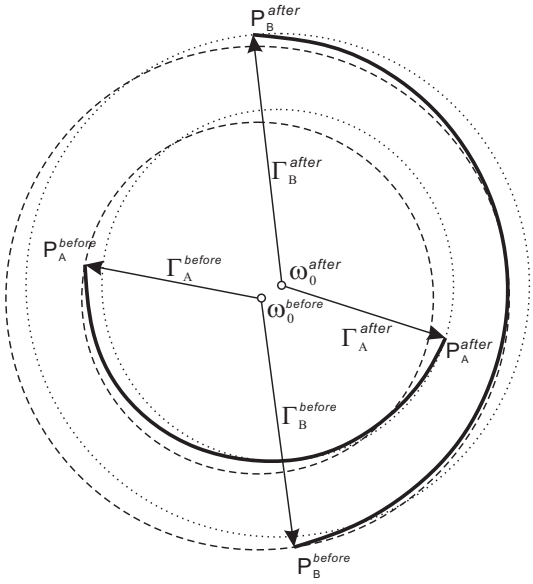

Fig. 5 Moving traces of EOAs P_A and P_B (P_C omitted) in space (*bold lines*) considering the precession-nutation and the polar motion of the Moon. From the beginning (*dashed lines*) to the end (*dotted lines*), the position of the rotation axis (center of the concentric circles) changes from $\boldsymbol{\omega}_0^{\rm before}$ to $\boldsymbol{\omega}_0^{\rm after}$ in space due to the precession and nutation. The change of position of the rotation axis in selenographic frame (i.e. the polar motion) causes the radius of the circles change from $\Gamma_A^{\rm before}$ ($\Gamma_B^{\rm before}$) to $\Gamma_A^{\rm after}$ ($\Gamma_B^{\rm after}$).

3.3 Polar Motion of the Moon

The librations at monthly period (a lunar day) or even shorter cause long period motion of the rotation axis in the selenographic reference frame and they are the polar motion of the Moon.

The polar motion of the Moon causes change of the angles between one of the directions of EOAs and the rotation axis of the Moon (Γ_A, Γ_B and Γ_C). In each data segmentation, i-th angle Γ_i are respectively

$$\Gamma_i = \cos^{-1}(-D_i) \quad i = A, B, C. \tag{5}$$

The change of Γ_i which caused by polar motion change within short data period can be respectively considered as

$$\Gamma_i = \Gamma_{i,0} + \dot{\Gamma}_i T \quad i = A, B, C. \tag{6}$$

$T = t - t_0$ is the time interval between each observational epoch and the central epoch. The radius at t_0 are $\Gamma_{i,0} (i = A, B, C)$.

Change of $\Gamma_i (i = A, B, C)$ means that the rotation axis moves in the selenographic frame (x_p, y_p). Thus x_p and y_p can be determined through

$$\begin{pmatrix} \cos\lambda' \cos\phi' \\ \sin\lambda' \cos\phi' \\ \sin\phi' \end{pmatrix} = \mathcal{R}_2(x_p)\mathcal{R}_1(y_p) \begin{pmatrix} \cos\lambda_0 \cos\phi_0 \\ \sin\lambda_0 \cos\phi_0 \\ \sin\phi_0 \end{pmatrix}. \tag{7}$$

(λ', ϕ') and (λ_0, ϕ_0) are the effective observer's position with respect to the rotation axis at the observational epoch and at the reference epoch respectively.

By expanding this formula and truncating to first order of variables x_p and y_p, it leads to

$$\phi' - \phi_0 = x_p \cos\lambda_0 - y_p \sin\lambda_0, \tag{8}$$

and

$$\lambda' - \lambda_0 = (x_p \sin\lambda_0 + y_p \cos\lambda_0) \cdot \tan\phi_0. \tag{9}$$

Obviously, they are the same as the equations of polar motion on the Earth.

As the latitude of the effective observers $\phi'_i = 90^\circ - \Gamma_i (i = A, B, C)$ are observable, we can build three equations on the latitude part as

$$\phi'_i(t) - \phi_{i,0} = x_p(t)\cos\lambda_{i,0} - y_p(t)\sin\lambda_{i,0}, \quad i = A, B, C. \tag{10}$$

However the absolute value of longitude of the effective observer is not estimable from direct observation. Alternatively, we can write their relative change between two effective observers in longitude as

$$\begin{aligned} P'_{ij}(t) - P_{ij,0} = {} & x_p(t)\,(\tan\phi_{i,0}\cdot\sin\lambda_{i,0} - \tan\phi_{j,0}\cdot\sin\lambda_{j,0}) \\ & + y_p(t)\,(\tan\phi_{i,0}\cdot\cos\lambda_{i,0} - \tan\phi_{j,0}\cdot\cos\lambda_{j,0})\,. \end{aligned} \tag{11}$$

where difference between two effective observers in longitude $P_{ij,0} = \lambda_{i,0} - \lambda_{j,0}$ ($\{i, j\} \in \{A, B, C \mid i \neq j\}$) are obtainable based on observable values Γ_i, Γ_j and fixed ξ_{ij} with the cosine rule of the spherical triangle as

$$\boldsymbol{P}_i \cdot \boldsymbol{P}_j = \cos\Gamma_i \cdot \cos\Gamma_j + \sin\Gamma_i \cdot \sin\Gamma_j \cdot \cos P_{ij} = \cos\xi_{ij}. \tag{12}$$

In this way, the position of the rotation axis in the selenographic frame can be determined from three latitude parameters of the effective observers and three parameters of difference in longitude between two effective observers. The geometric relation of polar motion is illustrated in Figure 6.

3.4 The Selenographic Reference Frame

To describe the reference coordinates of the three effective observers, we can define a temporary selenographic reference frame for the study of polar motion of the Moon.

Generally, we can choose any epoch (e.g. the first epoch of observation) as the reference epoch. The latitudes of the effective observers can be determined from values of the angles between the rotation axis and respective directions of EOAs at the reference epoch. The longitude of one effective observer can be arbitrarily given and the longitudes of the other two can be respectively determined through their difference in longitude with the first one.

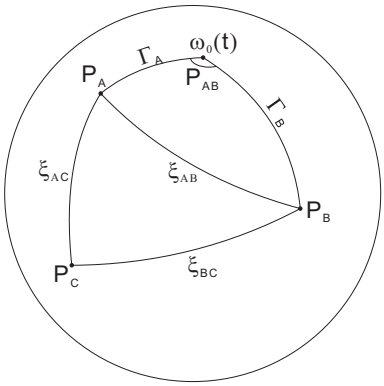

Fig. 6 The three effective observers (P_A, P_B and P_C) and the rotation axis of the Moon at a certain epoch $\boldsymbol{\omega}_0(t)$ in the selenographic reference frame. The geometry among them is also illustrated.

For example, we list the reference coordinates of the three effective observers in the temporary selenographic reference frame in Table 1. In the Table, $\lambda_{A,0}$ is the given value of the longitude of the first effective observer.

Although the selenographic coordinate of one point in the temporary frame can be different from the value in the conventional selenographic frame (constructed by laser retroreflectors in LLR, etc.), the definition of the temporary selenographic reference frame does not affect the study of the period, amplitude and secular drift of polar motion of the Moon.

4 SIMULATIONS

In this section, we test the principle of using the three FOV telescope to make observation of rotation of the Moon as well as other terrestrial planets like the Earth through computational simulations.

The pipeline of simulation work is Figure 7. First we simulate the CCD image taken by the three FOV telescope (Sect. 4.1) and test recognition of mixed stars from different FOVs. After recognition, the original CCD image at one epoch can be equivalently treated as three images taken by three isolated telescopes. Then the position of the central point of each one image in the celestial sphere are determined with a classical procedure of the astrometric image process respectively. The celestial position of the central point of the image is equal to the directions of the corresponding EOAs. Next, we use the method discussed in Sections 2 and 3 to solve the parameters of the planet's rotation. To be general and easily understood, the following simulation is based on virtual observation on the Earth in this section.

Table 1 Reference Coordinates of the Three Effective Observers in the Temporary Selenographic Reference Frame at the Reference Epoch

Station	Longitude	Latitude
A	$\lambda_{A,0}$	$90^\circ - \Gamma_{A,0}$
B	$\lambda_{A,0} + \cos^{-1}\left(\frac{\cos\xi_{AB} - \cos\Gamma_{A,0}\cdot\cos\Gamma_{B,0}}{\sin\Gamma_{A,0}\cdot\sin\Gamma_{B,0}}\right)$	$90^\circ - \Gamma_{B,0}$
C	$\lambda_{A,0} + \cos^{-1}\left(\frac{\cos\xi_{AC} - \cos\Gamma_{A,0}\cdot\cos\Gamma_{C,0}}{\sin\Gamma_{A,0}\cdot\sin\Gamma_{C,0}}\right)$	$90^\circ - \Gamma_{C,0}$

Table 2 Position of the Virtual Station, Directions of EOAs in Local Azimuthal Coordinate and Basic Angles in Data Preparation of the Simulation

Station position	$117\overset{\circ}{.}575$ E, $20\overset{\circ}{.}393$ N	focal length (fl)	1050 mm
Altitude	980 m	aperture	350 mm
Azimuth 0	266°	size of pixel (pscale)	12 μm
Height 0	35°	number of pixels	4096×4096
Azimuth 1	26°	size of FOV	$\sim 2\overset{\circ}{.}68$
Height 1	35°	magnitude limitation	9.0
Azimuth 2	146°		
Height 2	35°		
3 Basic angles	$90\overset{\circ}{.}37329$		

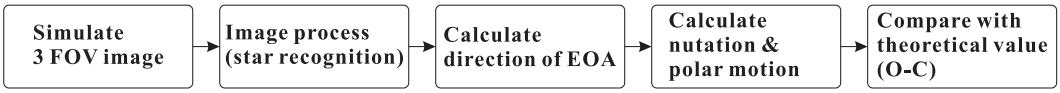

Fig. 7 Pipeline of the simulation work of virtual observation.

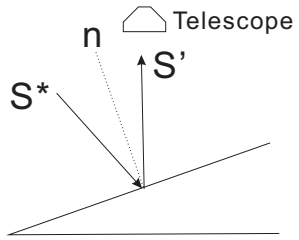

Fig. 8 To simulate the image of the three FOV telescope, star light is reflected by the mirror whose normal in TRF is $\boldsymbol{n}$. The original coordinate of one star in TRF is $\boldsymbol{S}^*$ and after being reflected, its light is received by the upside-down telescope as originating from $\boldsymbol{S}'$ in TRF. $\boldsymbol{S}' = 2(\boldsymbol{S}^* \cdot \hat{\boldsymbol{n}}_i)\hat{\boldsymbol{n}}_i - \boldsymbol{S}^*$.

4.1 Data Preparation

The time span of the simulated observation is from 1992 January 1 to 2013 November 25 which lasts 8000 days. The time interval between adjacent exposure in a day is one minute. In data preparation, the HIPPARCOS star catalog (Perryman et al. 1997) is used to provide the celestial coordinates of stars. We interpolate the daily Earth Orientation Parameters[1] (EOP 14 C04) from International Earth Rotation and Reference System Service (IERS) by cubic spline to each observational epoch within a day. The IAU2006 precession model, IAU2000 nutation model and procedures from IAU SOFA[2] under IERS 2010 conventions (Petit & Luzum 2010) are used to transfer the coordinates of stars from CRF to terrestrial reference frame (TRF). Influence from solid Earth tides, ocean tides and other minor geophysical phenomenon are temporally not included in simulation.

Parameters of position where the three FOV telescope is installed and the optical parameters of the virtual telescope are listed in Table 2. With the a-priori information on the deployment of the trihedron mirror set, the directions of three EOAs in the local azimuthal coordinate at the initial epoch are also listed in Table 2. The directions of three EOAs keep fixed in TRF in the simulation.

For a single star, suppose its position in TRF is $\boldsymbol{S}^*$. The telescope receives its reflected image (Fig. 8) whose coordinate in TRF $\boldsymbol{S}'$ is

$$\boldsymbol{S}' = 2(\boldsymbol{S}^* \cdot \hat{\boldsymbol{n}}_i)\hat{\boldsymbol{n}}_i - \boldsymbol{S}^*, \tag{13}$$

where $\hat{\boldsymbol{n}}_i$ is the normal of the mirror. To simulate the observational image of one FOV, star images possibly being in FOV are projected to the virtual CCD plate by gnomonic projection (Dick 1991). Changing the normal of the reflecting surfaces $i = 1, 2, 3$, the simulated image can be completed for the other two FOVs. The three images

[1] https://www.iers.org/IERS/EN/DataProducts/EarthOrientationData/eop.html

[2] http://www.iausofa.org

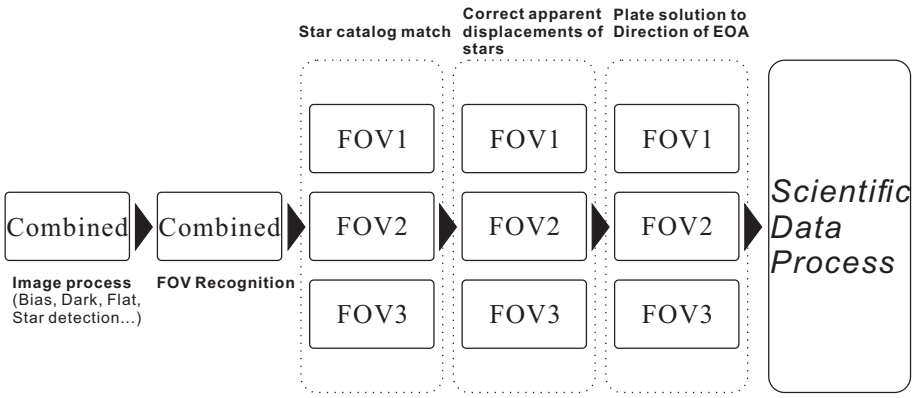

Fig. 9 Pipeline of image processing.

are then mixed together to complete the synthesized image which imitates the real observation. For other epochs, the simulated images can be synthesized in the same way.

4.2 Simulation: Determination of Directions of Three FOVs

We briefly introduce the main steps to determinate the celestial direction of EOA from the image of the three FOV telescope by Figure 9. Recognizing which FOV a certain star image comes from will be discussed in Section 4.3.

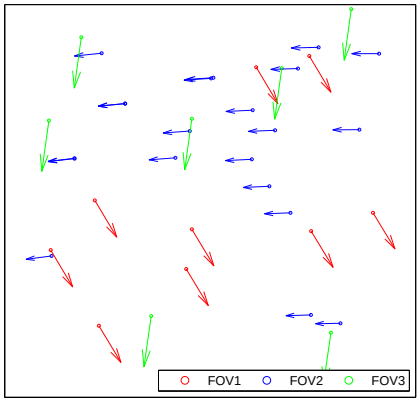

Fig. 10 Motion behavior of star images from different FOVs on CCD plate. The arrows represent velocities of motion of star images from FOV 1 (*red*), FOV 2 (*blue*) and FOV 3 (*green*) respectively.

For details of CCD image processing, readers can refer to Howell (2006) and Kovalevsky & Seidelmann (2004). In real observation, noise or uncertainty may exist in the surrounding environment, optical system, electronic system, etc. and they may influence the result of image processing. It is very hard to simulate their influence and we do not consider these influence facts in this simulation.

Table 3 Statistics of Motion Behavior of Star Images in Three FOVs

	Stars	v_x (pixel s^{-1})	v_y (pixel s^{-1})
FOV 1 (Red)	9	3.24 ± 0.02	-5.08 ± 0.03
FOV 2 (Blue)	18	-2.33 ± 0.06	-0.13 ± 0.08
FOV 3 (Green)	7	-0.93 ± 0.02	-6.24 ± 0.02

4.3 Simulation: Recognition of Mixed Star Images

Positions of the same star on the CCD plate will change with time due to the rotation of the Earth. Because directions of the EOAs of each FOVs are different in TRF, the moving direction of star images from different FOVs are different and can consequently be recognized.

The methodology in detail is presented in Sun et al. (2020). For example, the moving direction of the star images between two epochs in this simulation are illustrated in Figure 10 by arrows with different colors for different FOVs. In the simulation, because the focal length of the virtual telescope is long, the distortion of the image is not obvious. Hence, the motion behavior of the star images in each FOV agrees well from statistic study (Table 3).

To recognize this, one can set the threshold based on the statistic result. In the simulation, it is reasonable that all the stars can be automatically recognized.

If the motion behavior of star images in one field is diverse, which may exist in large distorted image, the threshold for recognition should be wider. In real observation, star images from different FOVs may be overlapping sometimes (the probability depends on the quantity of star images), which is another problem in the recognition. Thus some stars may not be successfully recognized in real observation.

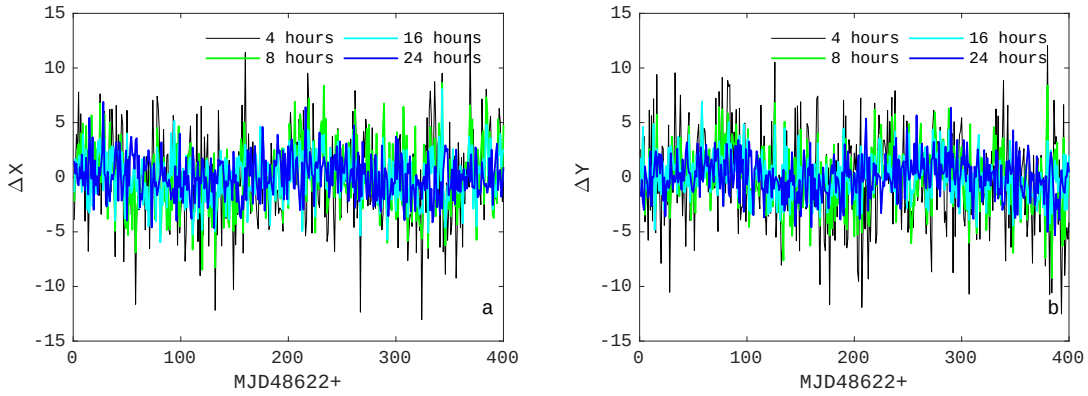

Fig. 11 Test of 400 days in which the time span of each data segmentation is all 1 hour and different lengths of observation data in each day are respectively studied. The deviation is the calculated directions of the rotation axis in CRF from their theoretical value from IAU2006 precession and IAU2000 nutation model epoch by epoch. a: X-component. b: Y-component. Unit: mas.

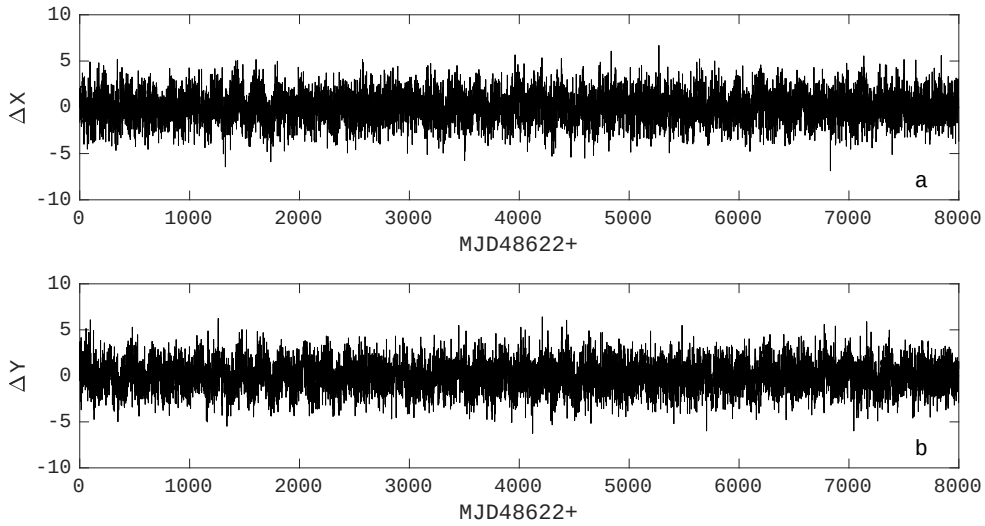

Fig. 12 Deviation of the calculated directions of the rotation axis in CRF from their theoretical value by IAU2006 precession and IAU2000 nutation model epoch by epoch. a: X-component. b: Y-component. Unit: mas.

4.4 Simulation: Data Process

4.4.1 Solution of the direction of the rotation axis in CRF

In this work, first we calculate the directions of the Earth's rotation axis in CRF once a day and then they are compared with the theoretical directions calculated from IAU2006 precession model and IAU2000 nutation model epoch by epoch.

A 400-day test is firstly made which evaluates how the length of data in each day and the sampling period of each data segmentation for calculation influences the deviation of the calculated direction of the Earth's rotation axis in CRF from the theoretical values.

Four different lengths of daily observational data series are chosen as 4 hours, 8 hours, 16 hours and 24 hours respectively and all are centered at UTC 12:00. They can simulate the general situation of real observation. The daily data series are all divided into data segmentations which last 1 hour each. Thus the 4 hours data series has four data segmentations, the 8 hours one has 8, and so on.

In each small data segmentation, which lasts only 1 hour, the observational equation is based on Equation (2) and the small motion of the pole happening during this period is considered as

$$X = X_0 + \dot{X}T \tag{14}$$

$$Y = Y_0 + \dot{Y}T \tag{15}$$

where T is the time interval between observational epoch and the central epoch of the certain segmentation. Then the results of each data segmentation in one day are used to fit

Equation (3) and Equation (4) to calculate the direction of the rotation axis of the Earth at UTC 12:00 of that day and compare with the theoretical values by IAU2006/2000 model. For other days, the calculation can be similarly done.

As Figure 11, the length of observational data accumulated in each day does not affect the deviation obviously. While the choice of the sampling period which is used to divide the daily observational data series into segmentations mostly depends on real situation of observation. The small change of the pole's position in space and its change in TRF which simultaneously influence determination of the center and the radius of the traces of EOAs are extremely difficult to distinguish only by observation data during a short time period like 1 hour or less. Theoretically the shorter time span of each data segmentation leads to less deviation when using Equation (2). On the other hand, the deviation of each data segmentation's calculation is sensitive to the quantity of data points and may influence the further calculation of values at UTC 12:00. Consequently, the 1 hour time span is a trade off in this case.

The formal result of computational simulation is presented for the case of 8000 days in total in which the length of daily observation data is from UTC 1:00 to UTC 23:00 and time span of each data segmentation is 1 hour. The directions of the rotation axis of the Earth at UTC 12:00 each day are by taking Equations (2), (14) and (15) in processing data segmentations and taking Equation (3) and Equation (4) in the processing value at UTC 12:00.

Deviation of our results from the theoretical directions of the rotation axis epoch by epoch are illustrated in Figure 12. If it represents daily deviations as $(O_i - C_i)$, the mean deviation for 8000 days is $\sqrt{\sum_i^{8000}(O_i - C_i)/8000}$. The mean deviation of both the X component and the Y component are 1.7 mas. After spectral analysis, it is shown that there is no obvious periodic fluctuation in the deviation series.

4.4.2 *Solution of the polar motion*

By the solution to observational data in each data segmentation, the angles between the rotation axis and the directions of EOAs $\Gamma_i (i = 1, 2, 3)$ can be determined. The angles at UTC 12:00 of each day are processed by Equation (6).

We follow the way described in Section 3.4 to determine the reference coordinates for the three effective observers. We let the longitude of the reference coordinate of the first $(i = 1)$ effective observer to be zero and the reference epoch takes the initial observational epoch (JD2457001.5). They are listed in Table 4.

Table 4 Reference Coordinates of the Three Effective Observers in the Temporary TRF in the Simulation (The Reference Epoch is at JD2457001.5)

i	Γ_i	longitude λ_i	latitude ϕ_i
1	$70\overset{\circ}{.}84077$	0°	$19^\circ 15923$
2	$21\overset{\circ}{.}18296$	$156\overset{\circ}{.}29533(P_{12})$	$68\overset{\circ}{.}81704$
3	$98\overset{\circ}{.}36549$	$87\overset{\circ}{.}47127(P_{13})$	$-8\overset{\circ}{.}36549$

The polar motion x_p and y_p are calculated with Equation (9) and Equation (10) and plotted in Figure 13. Its deviation from IERS EOP 14 C04 will be discussed in Section 4.4.3.

4.4.3 *Comparison of polar motion solution with IERS EOP*

Direct comparison between our polar motion result with IERS EOP 14 C04 is impossible because the reference longitudes of the three effective observers are arbitrary. However, it can make transformation between the two polar motion series.

The transformation model is

$$\begin{pmatrix} x'(t) \\ y'(t) \\ z'(t) \end{pmatrix} = \begin{pmatrix} x_0 \\ y_0 \\ z_0 \end{pmatrix} + (1+D)\mathcal{R}_1(\alpha)\mathcal{R}_2(\beta)\mathcal{R}_3(\gamma) \begin{pmatrix} x(t) \\ y(t) \\ z(t) \end{pmatrix}. \tag{16}$$

At each epoch, $(x(t), y(t), z(t))$ is the coordinate of the rotation axis in the temporary TRF, which is the result of Section 4.4.2. $(x'(t), y'(t), z'(t))$ is the coordinate of the rotation axis in ITRF. (x_0, y_0, z_0) are transfer parameters of the origin, (α, β, γ) are 3-axis rotation parameters and D is parameter of the scale.

The parameters of scale and transverse can be excluded and only needs to fit the parameters of net rotation. In the simulation, we select the whole polar motion series to estimate the rotation parameters by least square estimation. The results are $\alpha = 0\overset{\circ}{.}24643$, $\beta = -0\overset{\circ}{.}04174$ and $\gamma = -57\overset{\circ}{.}24768$ which defines the rotation angle from the temporary TRF to ITRF. By this transformation, we can get the reference coordinates of the three effective observers in ITRF now.

Figure 14 illustrates the deviation of our polar motion result from IERS EOP 14 C04 after transforming the (x_p, y_p) series into ITRF. The mean deviation of x_p and y_p components are 1.2 mas and 1.6 mas respectively. There are small fluctuations in the deviation series (amplitude less than 2 mas) at the Chandler period which may caused

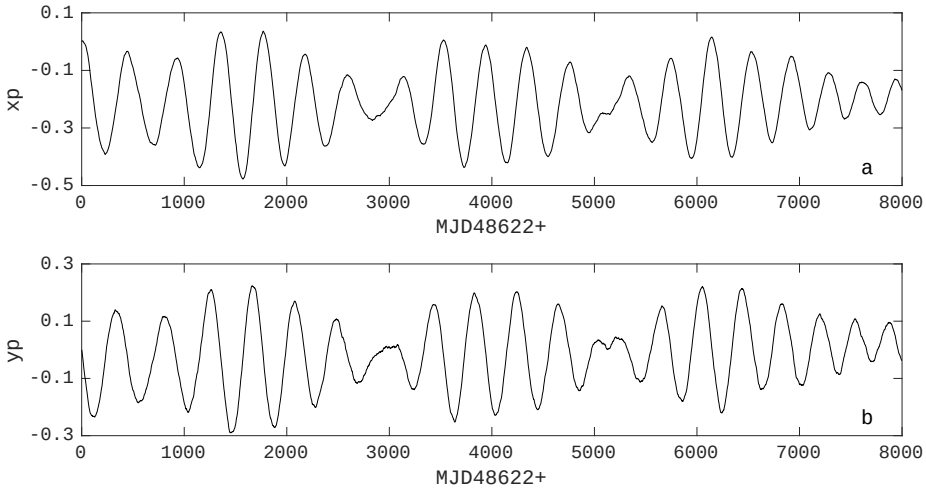

Fig. 13 Polar motion in the temporary TRF in this simulation. a: x_P component. b: y_P component. Unit: arcsec.

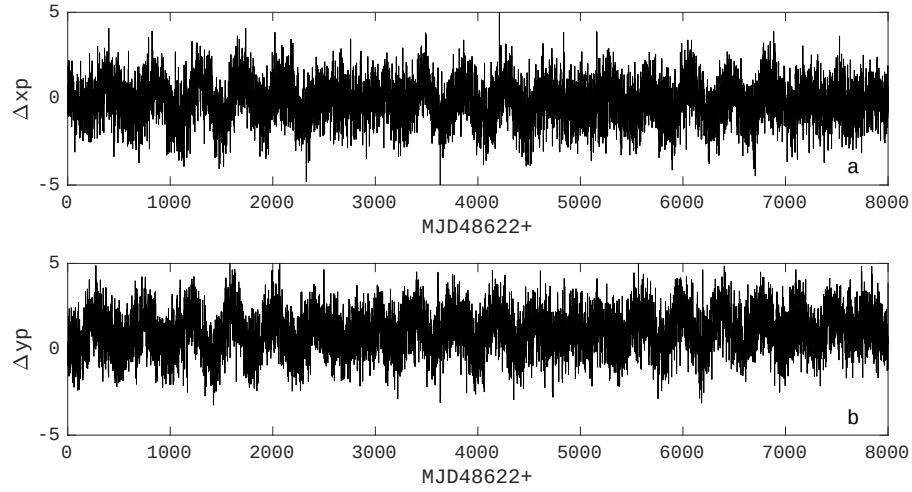

Fig. 14 Deviation of the calculated polar motion in ITRF from polar motion value in IERS EOPs. a: x_P component. b: y_P component. Unit: mas

by the transforming of the reference frame when making comparison with the IERS result.

5 SUMMARY AND DISCUSSION

This paper proposed a new method of observing the lunar physical libration using an in-situ three FOV telescope. Lunar physical librations are observed and studied by two groups of parameters, the precession-nutation and the polar motion. The simulation shows the precision of the observation with this telescope can reach the level of several mas. With absence of other in-situ observation on the rotation of the Moon currently, highly precise in-situ lunar physical libration data will be helpful to the scientific research on physics of the Moon.

Besides the concerned scientific objectives in this paper, improved information on lunar physical libration will also benefit future projects of lunar-based astronomical observation with better lunar ephemeris.

Historical research on the lunar physical libration and other science of the Moon will still be valuable in the new in-situ observation. In the current study, the crust of the Moon is suggested to be rigid. The influence of tidal deformed non-rigid crust on in-situ observation will be further studied. However the situation of real observation may differ a lot from the theoretical study because our knowledge on lunar science is still limited.

The engineering of the observational system is also important in this project. Questions about the way to keep the telescope firmly linked with the Moon's crust, thermal

protection of the system, selection of the station position on the Moon to apply the telescope, etc. are worth a lot of further study.

Last but not least, this telescope can also be applied to observe the rotation of other terrestrial planets like Mars.

Acknowledgements This work is supported by the National Natural Science Foundation of China (grant 11773058). Prof. Xinhao Liao is appreciated for long term firm support and helpful discussions.

References

Dick, W. R. 1991, Astronomische Nachrichten, 312, 113
Dickey, J. O., Bender, P. L., Faller, J. E., et al. 1994, Science, 265, 482
Folkner, W. M., Dehant, V., Le Maistre, S., et al. 2018, Space Sci. Rev., 214, 100
Hanada, H., Araki, H., Tazawa, S., et al. 2012, Science China Physics, Mechanics, and Astronomy, 55, 723
Howell, S. B. 2006, Handbook of CCD Astronomy, 5 (Cambridge, UK: Cambridge Univ. Press)
Huang, C., Jin, W., & Xu, H. 1999, Journal of Geodesy, 73, 125
Huang, C. L., Zhao, M., & Tang, Z. H., 2013, the 2013 Annual Meeting of Chinese Astronomical Society (Jiangsu: CAS)
Huang, C. L., Zhao, M., Qi, Z. X., et al. 2015, the 29th General Assembly of International Astronomical Union (Hawaii: IAU)
Kovalevsky, J., & Seidelmann, P. K. 2004, Fundamentals of Astrometry (Cambridge, UK: Cambridge Univ. Press)
Lindig, O., & Pannhorst, W. 1985, Appl. Opt., 24, 3330
Lognonné, P., & Johnson, C. 2007, Treatise on Geophysics, 10, 69
Perryman, M. A. C., Lindegren, L., Kovalevsky, J., et al. 1997, A&A, 500, 501
Petit, G., & Luzum, B. 2010, IERS conventions (2010), Tech. Rep. (Frankfurt am Main: Verlag des Bundesamts für Kartographie und Geodäsie)
Rambaux, N., & Williams, J. G. 2011, Celestial Mechanics and Dynamical Astronomy, 109, 85
Sun, L. Z., Huang, C. L., Yu, Y., et al. 2020, in preparation
Williams, J. G., Konopliv, A. S., Boggs, D. H., et al. 2014, Journal of Geophysical Research (Planets), 119, 1546
Zuber, M. T., Smith, D. E., Watkins, M. M., et al. 2013, Science, 339, 668